



Hydrous RuO₂-Decorated MXene Coordinating with Silver Nanowire Inks Enabling Fully Printed Micro-Supercapacitors with Extraordinary Volumetric Performance

Hongpeng Li, Xiran Li, Jiajie Liang,* and Yongsheng Chen

The fabrication of fully printable, flexible micro-supercapacitors (MSCs) with high energy and power density remains a significant technological hurdle. To overcome this grand challenge, the 2D material MXene has garnered significant attention for its application, among others, as a printable electrode material for high performing electrochemical energy storage devices. Herein, a facile and in situ process is proposed to homogeneously anchor hydrous ruthenium oxide (RuO₂) nanoparticles on Ti₃C₂T_x MXene nanosheets. The resulting RuO₂@MXene nanosheets can associate with silver nanowires (AgNWs) to serve as a printable electrode with micrometer-scale resolution for high performing, fully printed MSCs. In this printed nanocomposite electrode, the RuO₂ nanoparticles contribute high pseudocapacitance while preventing the MXene nanosheets from restacking, ensuring an effective ion highway for electrolyte ions. The AgNWs coordinate with the RuO₂@MXene to guarantee the rheological property of the electrode ink, and provide a highly conductive network architecture for rapid charge transport. As a result, MSCs printed from the nanocomposite inks demonstrate volumetric capacitances of 864.2 F cm⁻³ at 1 mV s⁻¹, long-term cycling performance (90% retention after 10 000 cycles), good rate capability (304.0 F cm⁻³ at 2000 mV s⁻¹), outstanding flexibility, remarkable energy (13.5 mWh cm⁻³) and power density (48.5 W cm⁻³).

sources^[4] due in part to their lengthy life span, high rate capability, and high power density.^[5,6] In general, effective strategies to define the interdigitated configuration of MSCs typically fall within two categories. The first category is based on conventional microfabrication technology, utilizing traditional silicon-based techniques such as photolithography and laser scribing.^[7,8] While these conventional microfabrication approaches have been successfully demonstrated for the fabrication of microdevices, the requisite processing conditions are not easily integrated into process flows conducive for flexible and wearable substrates. In light of these issues, significant effort has been put forth into developing the latter category of defining interdigitated configurations by printing the electrode materials in the form of a printable ink or gel.^[9] Holistically, when considering the limited footprint of a single device, the available capacitance and energy afforded by the electrode ink are the critical barrier hindering more widespread adoption of this technology.^[10] Furthermore, the proper printability and deposition

behavior of the printed electrode ink also play a critical role in defining the ultimate printed structure.^[11]

In the search for applicable candidates for printable MSC electrodes, MXene, a new family of 2D layered transition metal carbides or nitrides, has leapt to the forefront as a promising intercalation pseudocapacitor electrode material for energy storage.^[12–14] This material is derived from MAX phases, or layered hexagonal carbides and nitrides, where A is an

1. Introduction

The recent trend toward miniaturization and portability of electronic devices has rapidly advanced the development of microscale energy storage units.^[1–3] Micro-supercapacitors (MSCs), characterized in part by a planar interdigitated electrode, represent one specific class of these devices increasingly being leveraged as a competitive solution for on-chip power

H. Li, X. Li, Prof. J. Liang, Prof. Y. Chen
School of Materials Science and Engineering
National Institute for Advanced Materials
Nankai University
Tianjin 300350, P. R. China
E-mail: liang0909@nankai.edu.cn

The ORCID identification number(s) for the author(s) of this article can be found under <https://doi.org/10.1002/aenm.201803987>.

DOI: 10.1002/aenm.201803987

Prof. J. Liang, Prof. Y. Chen
Key Laboratory of Functional Polymer Materials of Ministry of Education
College of Chemistry
Nankai University
Tianjin 300350, P. R. China
Prof. J. Liang
Tianjin Key Laboratory of Metal and Molecule-Based Material Chemistry and Collaborative Innovation Center of Chemical Science and Engineering (Tianjin)
Nankai University
Tianjin 300350, P. R. China

A-group element (typically Al or Ga). MXene is obtained by etching away this A-group element from the MAX phase and is expressed by the general formula $M_{n+1}X_nT_x$ ($n = 1, 2, \text{ or } 3$), where M is an early transition metal (e.g., Sc, Ti, Zr, Hf, V, Nb, Ta, Cr, and Mo), X is either carbon or nitrogen, T represents surface terminations ($=O, -OH, \text{ and/or } -F$), and x is the number of functional termination groups.^[15,16] Although over 20 different MXene materials have been successfully realized to date, $Ti_3C_2T_x$ is the most commonly studied for electrochemical capacitor applications due to its high metallic conductivity (up to 6500 S cm^{-1}) for high current charge. Furthermore, because MXene nanosheets can facilitate intercalation of water and electrolyte ions between adjacent layers, $Ti_3C_2T_x$ can store charge through cation adsorption into swollen MXene galleries, accompanied and facilitated by rapid layer expansion and contraction.^[17] Due to the existence of surface functional terminations, the delaminated negatively charged $Ti_3C_2T_x$ nanosheets are highly hydrophilic, which enables $Ti_3C_2T_x$ to form a stable, viscous, and aqueous colloidal suspension or ink without the need for additional surfactant or polymer additives.^[18] The aforementioned attributes render MXene particularly attractive for printable miniaturized energy storage devices with high capacitances. However, like other 2D layered nanomaterials, MXene nanosheets also suffer from self-restacking and agglomeration during electrode fabrication due to the buildup of van der Waals forces between neighboring sheets. This restacking subsequently results in a loss of effective surface area accessibility of the electrolyte ion, greatly reducing the utilization of electrochemical reactions.^[19] To mitigate this issue in efforts to enhance the electrochemical performance of the MXene-based supercapacitors, techniques must be developed to restrain self-restacking to keep the MXene nanosheets separated within the electrodes.

One effective strategy for mitigating self-restacking is the introduction of molecular spacers between MXene layers, including, but not limited to manganese oxide,^[20,21] carbon nanotubes,^[22,23] graphene,^[24,25] and polypyrrole.^[26,27] These interspaced layers increase the number of accessible electroactive sites and greatly improve the accessibility of electrolyte ions. Numerous recent studies have demonstrated that the functional surface of MXene facilitates the adsorption of metal oxides and metal hydroxides and, in turn, resulting in more sufficiently electrochemically active species on the conductive MXene surface.^[28] This in situ growth and uniform anchoring of fine nanomaterials on the MXene surface is a feasible and promising solution to reduce agglomeration and restacking of MXene nanosheets while retaining their hydrophilic and printable nature.

In this work, we report on a fully printed strategy to assemble flexible MSCs by printing thixotropic nanocomposite inks for interdigitated electrodes comprising $RuO_2 \cdot xH_2O @ Ti_3C_2T_x$ (MXene) nanosheets and silver nanowires (AgNWs). The $RuO_2 \cdot xH_2O @ MXene$ nanocomposite was synthesized through a simple aqueous-phase synthetic process. In the nanocomposite, the amorphous, hydrous RuO_2 nanoparticles contribute high pseudocapacitance and serve as spacers to effectively support adjacent nanosheets to promote the transfer of electrons from MXene to RuO_2 nanoparticles, while establishing an expanded ion highway for electrolyte

ions. The 1D AgNWs coordinate with the 2D $RuO_2 \cdot xH_2O @ MXene$ nanosheets to ensure high viscosity and suitable rheological behavior for the electrode ink without the additional of other inactive additives. On a macroscale, the continuous AgNW network in the printed electrodes forms highly conductive electron pathways to promote charge transfer while maintaining a compliant structure to accommodate bending strains. The resultant screen-printed MSCs based on this $RuO_2 \cdot xH_2O @ MXene-AgNW$ nanocomposite ink exhibit a landmark volumetric capacitance of 864.2 F cm^{-3} at a scan rate of 1 mV s^{-1} , high rate capacity (up to 2000 mV s^{-1}), excellent cycle stability (90% retention after 10 000 cycles), and outstanding flexibility (87.3% retention after 2000 bending cycles with bending strain of 5%). These performance metrics highlight the potential for MXene in miniaturized energy storage devices and foreshadow their applicability for a multitude of other devices.

2. Results and Discussion

RuO_2 nanoparticles can be introduced and anchored onto the MXene nanosheets through the facile in situ synthetic process depicted in **Figure 1**. In a typical synthesis, delaminated MXene nanosheets were prepared by selectively etching bulk Ti_3AlC_2 , followed by subsequent exfoliation (Figure 1a). Following exfoliation, hydrous RuO_2 nanoparticles were deposited in situ on the MXene nanosheets by admixing a $RuCl_3$ solution into a well-dispersed MXene suspension. This deposition process was enabled by the presence of hydrophilic oxygen-containing functional groups on the MXene surface which serve as a surfactant to ruthenium chloride, allowing the positively charged Ru^{3+} to adsorb onto the negatively charged MXene surface through electrostatic interactions.^[29] Following deposition of the Ru ions, hydrous RuO_2 nanoparticles were subsequently formed through oxidation of the Ru^{3+} . These RuO_2 nanoparticles were anchored in situ onto the surface of the MXene via strong chemical interactions between the residual oxygen-containing functional groups on the MXene and hydrous RuO_2 or through van der Waals interactions between the MXene and the nanoparticles.^[29,30] These interactions effectively limit the self-growth and spontaneous agglomeration of $RuO_2 \cdot xH_2O$,^[31,32] resulting in monodispersed RuO_2 nanoparticles decorated on the nanosheets. The resulting $RuO_2 \cdot xH_2O @ MXene$ nanocomposite was formulated along with a AgNW solution to yield a gel-like, printable ink.^[33,34] The mass ratio between $RuO_2 \cdot xH_2O @ MXene$ and AgNWs was optimized to be 0.75:1 (as detailed in the Experimental Section and the Supporting Information) and is subsequently denoted as R@M-A_{0.75:1}. For comparison purposes, pure MXene ink, MXene and AgNW nanocomposite ink (M-A ink), and a nanocomposite ink comprising $RuO_2 \cdot xH_2O$ nanoparticles, MXene and AgNWs (R-M-A ink), admixed with no additional processing were also fabricated. Following ink formulation, the flexible MSCs were fabricated by directly screen printing the electrode inks onto a paper substrate (average aperture size of $0.45 \mu\text{m}$ and thickness $\approx 90 \mu\text{m}$, Haining Zhongli Filtering Equipment Factory) through a precision stainless-steel screen mesh. A gel electrolyte was drop-cast onto the project area of

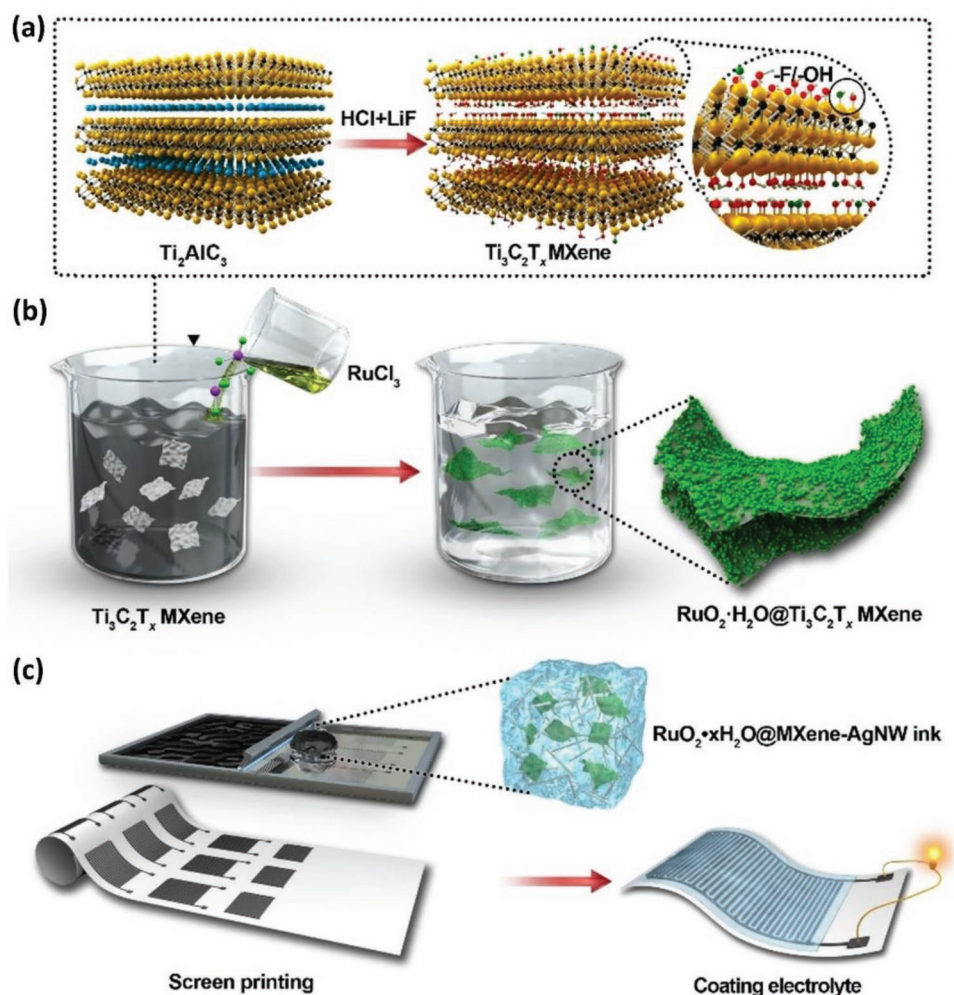


Figure 1. Schematic illustration of a) the synthesis process of $Ti_3C_2T_x$ MXene, b) the process used for the synthesis of $RuO_2 \cdot xH_2O@MXene$ nanocomposite, and c) the fabrication processes for screen-printed flexible MSC devices.

the microelectrodes as the final step (see details in the Experimental Section).

To elucidate more information about the ink formulation, various characterizations were conducted at different steps of the process flow. Transmission electron microscopy (TEM) images of thin, transparent MXene nanosheets are illustrated in **Figure 2a**, with the corresponding selected area electron diffraction (SAED) pattern depicting a well-defined hexagonal crystal symmetry structure, aligning with previously reported data.^[19,35] The atomic force microscopy (AFM) characterization shown in **Figure 2b** measures the thickness of MXene nanosheet at ≈ 1.5 nm and the lateral size of the nanosheets at 2–5 μm (**Figure 2c**; **Figure S1a**, Supporting Information), confirming the successful exfoliation of Ti_3AlC_2 MAX into monolayers.^[36,37] Further information can be garnered from the electron microscopy images of the $RuO_2 \cdot xH_2O@MXene$ nanocomposite. The TEM (**Figure 2d**) and scanning electron microscopy (SEM; **Figure S1b**, Supporting Information) images show the $RuO_2 \cdot xH_2O$ nanoparticles homogeneously anchored onto the surface of the MXene nanosheets. This homogenous anchoring of the $RuO_2 \cdot xH_2O$ nanoparticles is

afforded by the hydrophilic nature of MXene, allowing the nanosheets to effectively position the $RuO_2 \cdot xH_2O$ nanoparticles during synthesis, subsequently leading to the formation of well-dispersed $RuO_2 \cdot xH_2O$ nanoparticles.^[38] The high-resolution TEM (HRTEM) image in **Figure 2e** indicates a lattice spacing of 0.18 nm for the (211) lattice plane of hydrous RuO_2 , with the discontinuous lattice fringes highlighting the polymorphic and amorphous characteristics of the obtained RuO_2 nanoparticles. In addition, the elemental mapping of the TEM image (**Figure S1c**, Supporting Information) shows a uniform distribution of C, Ti, O, and Ru over the nanocomposite, further pointing to the homogeneous distribution of $RuO_2 \cdot xH_2O$ nanoparticles on the MXene nanosheets.

X-ray diffraction (XRD) was used to quantify the differences in interlayer spacing arising from the anchoring of the $RuO_2 \cdot xH_2O$ nanoparticles. An intense (002) diffraction peak at around 6.5° is observed in the XRD pattern of the pure MXene in **Figure 2f**, corresponding to an interlayer spacing of ≈ 1.4 nm. After a simple blending with the $RuO_2 \cdot xH_2O$ nanoparticles, no apparent change of the (002) diffraction peak was observed

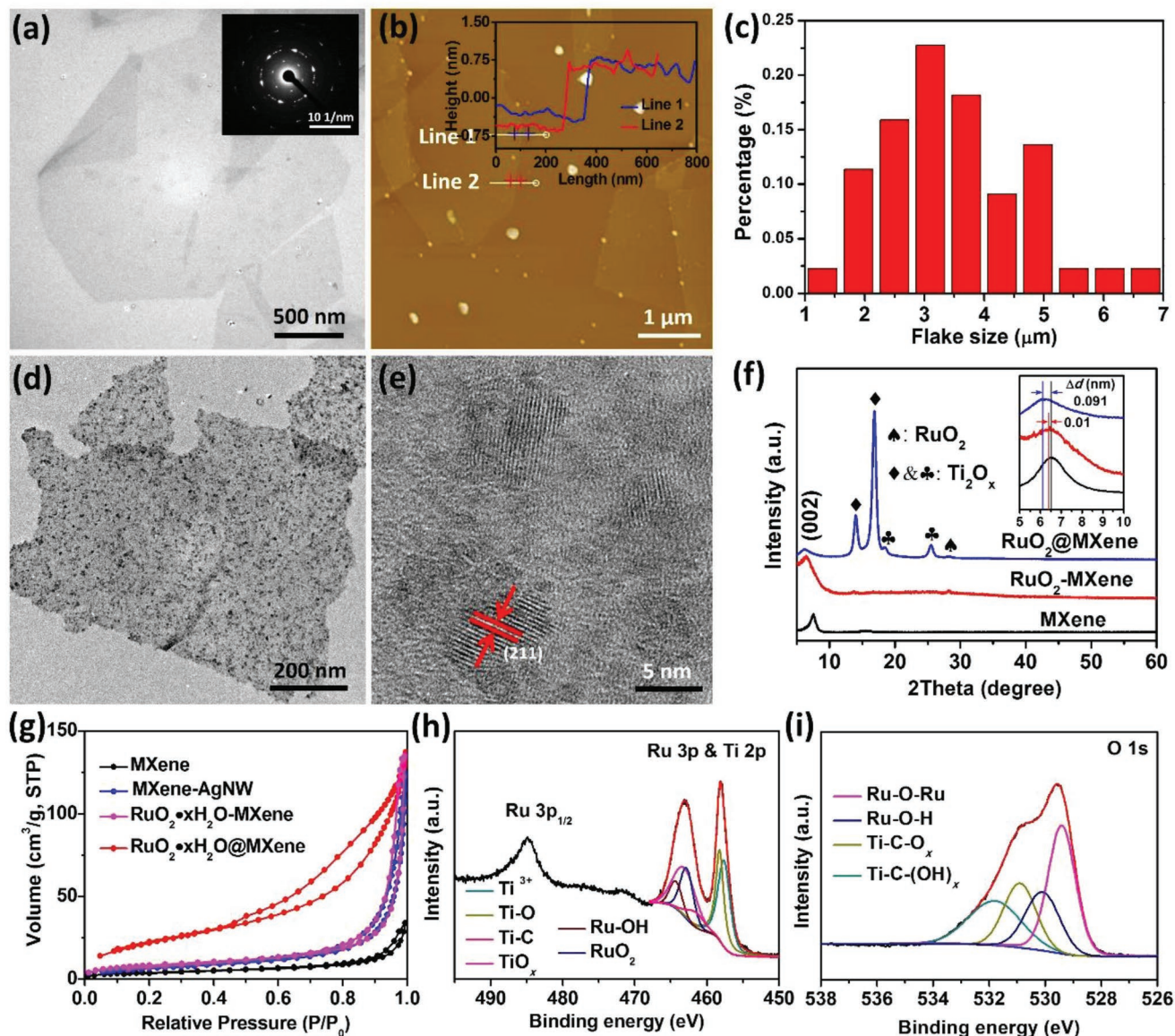


Figure 2. a) TEM image of delaminated $\text{Ti}_3\text{C}_2\text{T}_x$ MXene nanosheets. SAED pattern is included in the inset. b) AFM image of MXene nanosheets, with corresponding height profile along the crossed line in the inset. c) The lateral size distribution of MXene nanosheets. d) TEM and e) HRTEM images of the $\text{RuO}_2 \cdot x\text{H}_2\text{O}@\text{MXene}$ nanocomposite. f) XRD patterns of the pure MXene, $\text{RuO}_2 \cdot x\text{H}_2\text{O}-\text{MXene}$, and $\text{RuO}_2 \cdot x\text{H}_2\text{O}@\text{MXene}$ nanocomposites. The inset shows the (002) diffraction peaks of the MXene, $\text{RuO}_2 \cdot x\text{H}_2\text{O}-\text{MXene}$, and $\text{RuO}_2 \cdot x\text{H}_2\text{O}@\text{MXene}$ nanocomposites, with the numbers corresponding to the d -spacing difference between MXene and the other two nanocomposite. g) Nitrogen adsorption–desorption isotherms of MXene, MXene–AgNW, $\text{RuO}_2 \cdot x\text{H}_2\text{O}-\text{MXene}$ nanocomposite, and $\text{RuO}_2 \cdot x\text{H}_2\text{O}@\text{MXene}$ nanocomposite. High-resolution XPS spectra of h) Ti 2p and Ru 3p spectra, and i) O 1s of the $\text{RuO}_2 \cdot x\text{H}_2\text{O}@\text{MXene}$ nanocomposite.

for the $\text{RuO}_2 \cdot x\text{H}_2\text{O}-\text{MXene}$ nanocomposite. In contrast, the XRD pattern of the $\text{RuO}_2@\text{MXene}$ nanocomposite exhibited a clear shift downward in the (002) peak from $\approx 6.5^\circ$ to $\approx 6.1^\circ$, corresponding to an increase of 0.09 nm in the spacing between MXene layers (inset in Figure 2f). This increase in spacing indicates that the anchored hydrous RuO_2 nanoparticles can efficiently expand the interlayer spacing of MXene nanosheets, which facilitates the diffusion and transport of electrolyte ions during the charge/discharge process. Furthermore, the diffraction peaks located at 14° , 16.7° , 18.3° , and 25.4° for $\text{RuO}_2 \cdot x\text{H}_2\text{O}@\text{MXene}$ nanocomposite highlight the presence

of titanium oxide, which may result from the oxidation of Ti during the preparation process.^[39] The low intensity and broad diffraction peak at 28.3° is attributed to the low crystallinity, hydrous RuO_2 .^[40,41]

In efforts to further characterize the $\text{RuO}_2 \cdot x\text{H}_2\text{O}@\text{MXene}$ nanocomposite, the nitrogen (N_2) adsorption–desorption measurement was utilized to validate the mitigation of restacking structures in the nanocomposite (Figure 2g). The N_2 adsorption–desorption isotherm of $\text{RuO}_2 \cdot x\text{H}_2\text{O}@\text{MXene}$ nanocomposite exhibits type IV characteristics with a clear H3 hysteresis loop in the pressure range of 0.45–1.0, indicating the presence of mesoporosity

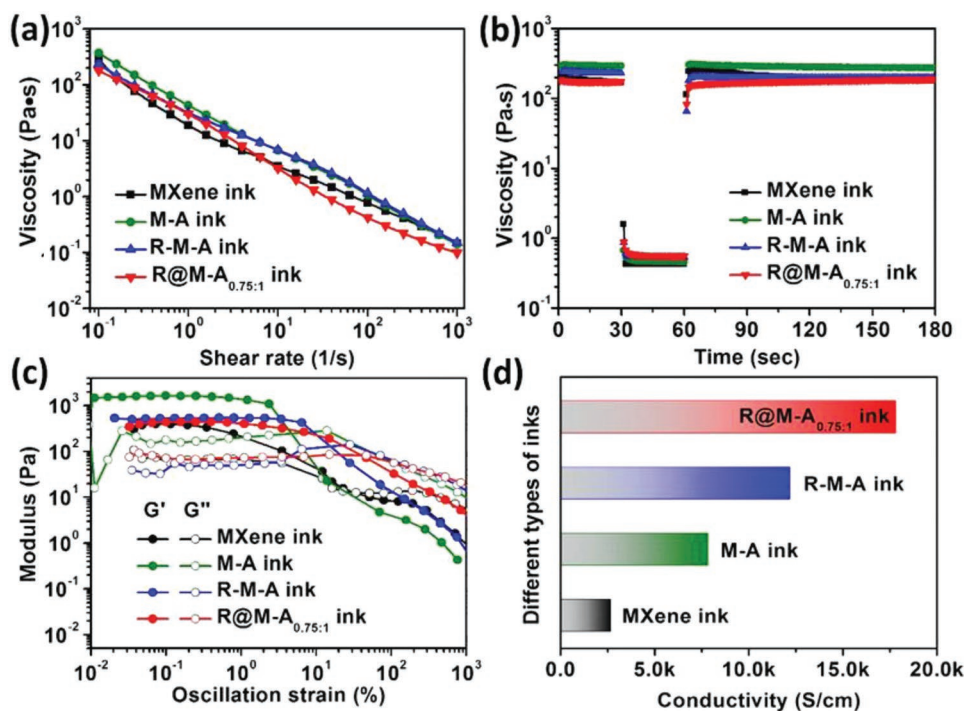


Figure 3. a) Viscosity as a function of shear rate for pure MXene ink, M-A ink, R-M-A ink, and R@M-A_{0.75:1} ink. b) Rheological behavior of the electrode inks during the screen-printing process. c) Variation of G' and G'' as a function of oscillation strain. d) Electrical conductivities of as-prepared electrodes screen-printed from the electrode inks.

and slit-shaped pores.^[42,43] The Brunauer–Emmett–Teller (BET) specific surface area of RuO₂·xH₂O@MXene nanocomposite is calculated to be 83.1 m² g⁻¹, which is much larger than that of pure MXene (14.7 m² g⁻¹), MXene–AgNW (33.9 m² g⁻¹), and RuO₂·xH₂O–MXene nanocomposite (46.4 m² g⁻¹). These results strongly suggest that the in situ anchored RuO₂·xH₂O nanoparticles on the separated MXene surface can effectively hinder the restacking of MXene nanosheets after the removal of solvents. The pore size distribution (Figure S2, Supporting Information) suggests that the RuO₂·xH₂O@MXene nanocomposite consists of macropores originating from the channel pores derived from the RuO₂·xH₂O nanoparticles between MXene nanosheets. The resulting increase in surface area and mesoporous structure of the RuO₂·xH₂O@MXene nanocomposite becomes favorable with regard to acceleration of the transport and diffusion of electrolyte ion, which in turn is favorable in terms of improvement of the electrochemical performance.

To confirm the surface chemical state of the nanocomposite, X-ray photoelectron spectroscopy (XPS) was used to analyze the sample. As shown in Figure 2h, the Ti 2p spectrum can be deconvoluted into four peaks representing Ti³⁺ (457.6 eV), Ti–O (458.2 eV), Ti–C (461.5 eV), and TiO_x (463.1 eV, 1.5 < x < 2).^[44–46] The Ru 3p_{3/2} peak can be deconvoluted into two separate peaks: RuO₂ at 462.8 eV and Ru–OH at 464.3 eV.^[47,48] The O 1s XPS spectrum taken from the sample is depicted in Figure 2i and can be broken down into a Ru–O–Ru peak located at 529.4 eV, a Ru–O–H peak located at 530.1 eV, a Ti–C–O_x peak at 530.9 eV, and a Ti–C–(OH)_x peak at 531.8 eV.^[47,49] These spectroscopic results further confirm that the hydrated RuO₂ nanoparticles are successfully anchored and integrated onto the MXene sheets.

Following material characterization, rheological tests were conducted at ambient temperature to characterize the properties of the printable electrode inks. As shown in Figure 3a, the apparent viscosity of MXene ink, M-A ink, R-M-A ink, and R@M-A_{0.75:1} ink at a shear rate of 0.1 s⁻¹ is 288.2, 371.7, 234.4, and 179 Pa s, respectively. These viscosities decrease linearly with increasing shear rates, indicating the ideal shear-thinning behavior observed in non-Newtonian fluids. This behavior enables the continuous extrusion of ink through the screen mesh under moderate conditions.^[50] For further rheological characterization, peak hold step (PHS) measurements with shear rates and time intervals simulating the actual screen-printing process were conducted. For all inks, a sudden decline in viscosity was observed when the shear rate increased from 0.1 to 200 s⁻¹. Following this decline in viscosity, a rapid reversion back to its original viscosity was observed as the shear rate recovered to 0.1 s⁻¹ (Figure 3b). This high elasticity ensures the structural integrity of the printed features, which in turn enables the printing of fine lines at a high resolution.^[51,52] To further probe the rheological behavior, the storage modulus (G') and loss modulus (G'') as a function of oscillation strain for the ink were tested, and is depicted in Figure 3c. All of the tested screen-printed inks exhibit a solid-like behavior (characterized by $G' > G''$) before their yield stress. The solid-like behavior exhibited in this region is beneficial for solidification of the inks during the screen-printing process. After the yield point, the storage modulus decreases more than that of the loss modulus ($G'' > G'$), suggesting viscous characteristics dominate, resulting in liquid-like behavior in the high shear stress region. When translated to actual printing conditions, this behavior

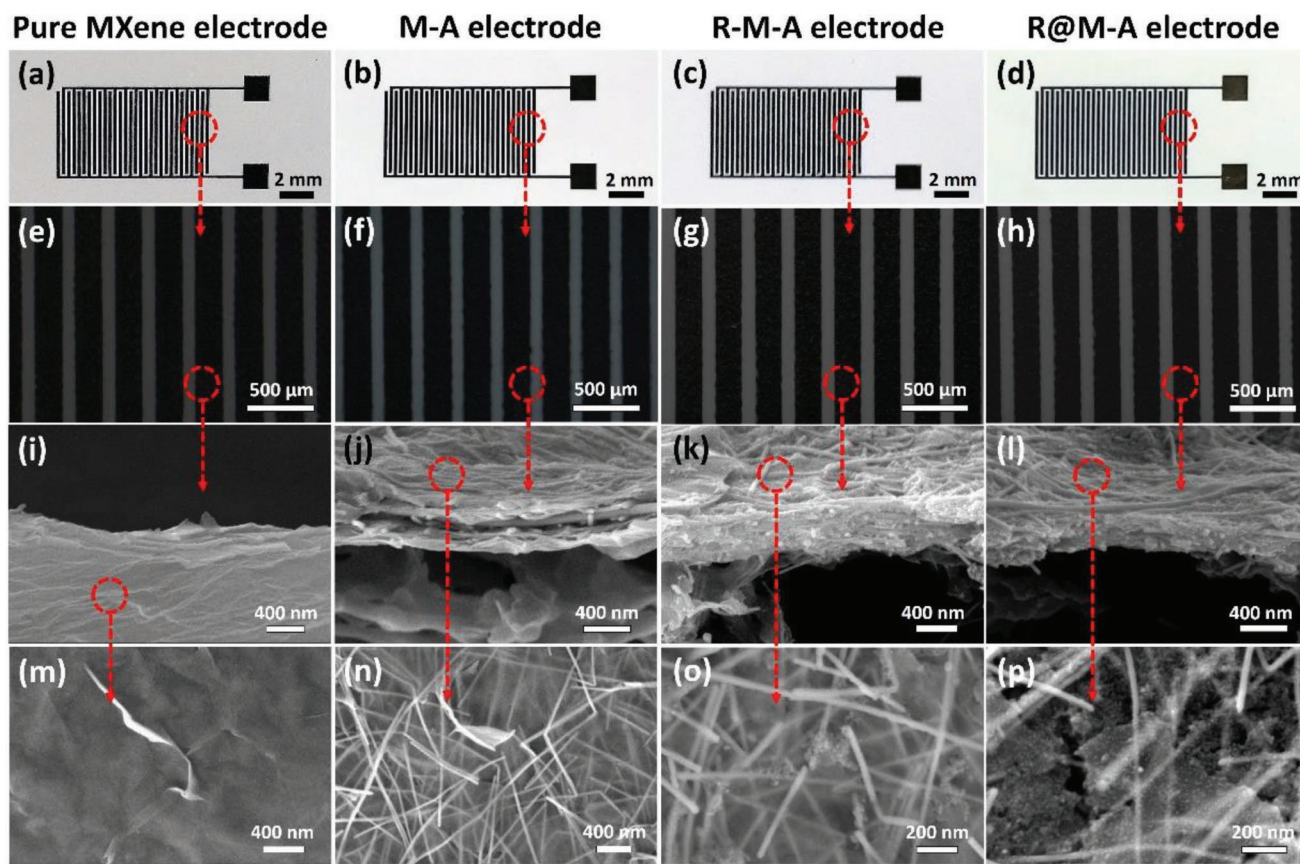


Figure 4. Optical images and optical microscopy images of a,e) pure MXene MSC, b,f) M-A MSC, c,g) R-M-A MSC, and d,h) R@M-A_{0.75:1} MSC. Cross-section and top-view SEM images of i,m) pure MXene MSC, j,n) M-A MSC, k,o) R-M-A MSC, and l,p) R@M-A_{0.75:1} MSC.

enables the ink to be smoothly extruded through the screen mesh at high shear stresses, while still retaining the printed architectures after the printing process. As a result, the MXene ink, M-A ink, R-M-A ink, and R@M-A_{0.75:1} inks were found to exhibit the appropriate viscosity and shear-thinning property for screen printing.

After rheological characterization, the electrical properties of the inks were analyzed. The conductivity of the R@M-A_{0.75:1} ink after printing and drying under ambient condition was measured to be as high as $17\,800\text{ S cm}^{-1}$ (Figure 3d). This high conductivity is due in part to the presence of the highly conductive AgNW network and the small size of RuO₂@MXene nanocomposite sheet treated by ultrasonic during the dispersing process. To support this theory, the conductivity of R@M-A_{0.75:1} was compared against other inks, and found to be much higher than that of the MXene ink (2653 S cm^{-1}), M-A ink (7830 S cm^{-1}), and R-M-A ink ($12\,182\text{ S cm}^{-1}$). Furthermore, the conductivity of the R@M-A_{0.75:1} ink is also higher than previously reported printed interdigital electrodes for MSCs to date.^[9,53–55] This high conductivity enables the printed structure to function as both the electrode and current collector in the MSCs.

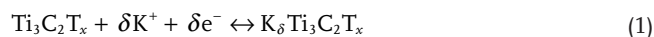
Proceeding sequentially through the manufacturing process, quantification and characterization of the printed lines were conducted following characterization of the base ink. The characterization of the base ink detailed above is critical, as it determines the ultimate printability of the ink. With optimized

printability of the inks, the R@M-A_{0.75:1} ink was able to enable a printing resolution of the electrode lines of $\approx 50\text{ }\mu\text{m}$ without the use of additional organic binders or additives (Figure S3, Supporting Information). The printing resolution is detailed in Figure 4a–d, with optical images depicting a typical MSC screen-printed from pure MXene ink, M-A ink, R-M-A ink, and R@M-A_{0.75:1} ink, respectively. Zoomed-in optical microscope images in Figure 4e,h reveal that the width of the printed finger electrodes for all pure MXene, M-A, R-M-A, and R@M-A_{0.75:1} MSCs was $\approx 200\text{ }\mu\text{m}$ with the interspace distance between the adjacent finger electrodes $\approx 100\text{ }\mu\text{m}$. These well-defined shapes and uniform edges of the isolated finger electrodes help mitigate the potential for shorting of the devices, thus improving the printing reliability.

For more in-depth characterization, microstructures of all the printed finger electrodes were characterized by cross-sectional (Figure 4i–l) and top-view SEM (Figure 4m–p). The cross-sectional SEM image in Figure 4i shows a layered, but dense structure of the pure MXene electrode. This restacking observed in the MXene nanosheets restricts the electrolyte ions from permeating into the electrode, resulting in a low electrode utilization and lower rate capability for the MSC device utilizing the electrode. In contrast to this restacking observed in the pure MXene electrode, the cross-sectional SEM image of the M-A MSC electrode made with MXene nanosheets with AgNWs shows an alternately stacked structure (Figure 4j), which is

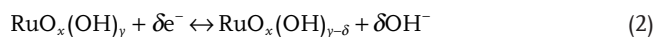
beneficial for electrolyte transportation.^[56] A top-down view of the M-A MSC electrode is illustrated in Figure 4h, depicting a uniformly distributed AgNW network. After introducing hydrous RuO₂ nanoparticles to the system by simply admixing components, the screen-printed electrode based on R-M-A ink exhibits a densely uniform and compact structure (Figure 4k) as a result of the RuO₂ nanoparticles occupying the voids between the 3D networks formed by the AgNWs and MXene. However, as a result of no additional processing to uniformly adhere the RuO₂ to the MXene, significant aggregation of the RuO₂ nanoparticles is observed in the R-M-A MSC electrode (Figure 4o). This aggregation brings about detrimental effects on the electrochemical performance of RuO₂ nanoparticles due to the incomplete reaction of RuO₂ during the electrochemical redox process. This reaction proceeds from the surface of the RuO₂ particles and progressively slows as the reaction proceeds.^[57] To mitigate aggregation of the RuO₂ nanoparticles, the aqueous-phase synthetic process to uniformly adhere RuO₂ to the MXene nanosheets was used to make the R@M-A_{0.75:1} MSC microelectrode (Figure 4l). A dense electrode structure with a thickness of ≈0.27 μm is still observed, ensuring high electrical conductivity of the electrode and efficient charge transport between the nanocomponents. However, with the additional processing, the fine RuO₂ nanoparticles are homogeneously dispersed on the surface of the MXene without visible aggregation (Figure 4p). These monodispersed RuO₂ nanoparticles not only serve as nanopacers to prevent the MXene from restacking, which enhance the utilization of active materials during Faradic reactions but also contribute high pseudocapacitance.

Proceeding sequentially again through the manufacturing process, the electrochemical performance of the final assembled screen-printed MSCs was investigated using polyvinyl alcohol (PVA)-KOH as a gel electrolyte. The electrochemical performance is displayed in Figure 5a through a comparison of cyclic voltammetry (CV) curves of the four configurations of MXene-based MSCs scanned at a scan rate of 100 mV s⁻¹. All four CV curves exhibit symmetrical rectangular shapes with no distinctive peaks, demonstrating ideal capacitive behavior during charging and discharging at a pseudoconstant rate over the complete voltammetric cycle.^[58] This ideal capacitive behavior is attributed to the surface electrosorption of electrolyte cations as well as the Faradaic pseudocapacitance of the continuous and reversible redox reactions on the surface of the Ti₃C₂T_x nanosheets. In turn, these redox reactions are dependent on the electrochemical intercalation/deintercalation of alkali cations (K⁺) during the rapid charge/discharge processes.^[15,59] In a simplified view, the electrochemical reaction can be represented as follows



Because of the introduction of highly electrically conductive AgNWs into the MXene layer, the response current of M-A MSC is larger than that of MXene MSC. This amalgamation of materials suppresses the restacking of MXene nanosheets, thereby decreasing the overall resistance of the screen-printed electrode. This in turn increases the utilizable surface area for the electrolyte ion. In addition to a higher response current,

higher CV integration areas for R-M-A MSC and R@M-A MSC can also be seen after the introduction of RuO₂·xH₂O nanoparticles. This phenomenon stems from the pseudocapacitance of hydrous RuO₂ in alkaline electrolyte and can be expressed as^[60]



A distinction is also observed between inks with the hydrous RuO₂ uniformly adhered on the MXene surface, and those merely admixed together. When contrasted with the R-M-A MSC, the R@M-A_{0.75:1} MSC exhibits a larger response current and CV integral area, indicating a higher charge storage capability. However, a further increase of the amount of RuO₂·xH₂O in the nanocomposite will compact the electrode (Figure S4, Supporting Information) and visibly reduce the electrical conductivity of the printed electrode of the R@M-A MSC (Figure S5, Supporting Information). This reduction of conductivity results in inferior electrochemical properties (Figures S6 and S7, Supporting Information), highlighting the threshold for addition of the nanoparticles. The specific volumetric capacitances of the MXene MSC, M-A MSC, R-M-A and R@M-A_{0.75:1} MSC obtained at 5 mV s⁻¹ are 76.8, 119.7, 449.2, and 821.0 F cm⁻³, respectively (Figure 5b). Remarkably, the R@M-A_{0.75:1} MSC could deliver a high volumetric capacitance value of 864.2 F cm⁻³ at 1 mV s⁻¹, which is the highest recorded value for MXene-based MSCs^[6,10,24,36,61] (Figure 5c; Table S1, Supporting Information) and printed MSCs^[62] (Table S2, Supporting Information). More importantly for practical applications, the specific volumetric capacitance of R@M-A_{0.75:1} MSC has a rate capability of 37%, maintaining a capacitance of 304.0 F cm⁻³ at 2000 mV s⁻¹. This rate capability exceeds those of pure MXene MSC (17.1%) and R-M-A (32.6%), with the improvement in rate performance attributed to the AgNW networks. These networks enable rapid transportation of released electrons during the charging and discharging processes, resulting in the high rate performance.

To further illuminate the kinetics of electron and ion transport within the screen-printed MSCs, electrochemical impedance spectroscopy (EIS) was conducted at a frequency ranging from 0.01 Hz to 100 kHz. As shown in Figure 5d, the Nyquist plots of the different inks all exhibit similar curves, including a squashed semicircle in the high frequency region, and an approximately vertical line in the low-frequency region. In the high frequency region, the diameters of the semicircle for the M-A MSC, R-M-A MSC and R@M-A_{0.75:1} MSC are smaller than that of the pure MXene MSC, indicating that the charge transfer resistance (*R*_{ct}) was decreased and the ionic conductivity improved after the embedding of the AgNWs.^[63] In addition, the slopes of the plots in the low-frequency regions of M-A MSC, R-M-A MSC, and R@M-A_{0.75:1} MSC are significantly greater than that of the MXene MSC, indicating their lower diffusion resistances.^[19] The improved ion transport behavior in inks with AgNWs is attributed largely in part to the embedded nanowires, which can provide more electrolyte permeable active sites. The minimum resistance and optimal capacitance behavior of the R@M-A_{0.75:1} MSC was obtained by anchoring small RuO₂·xH₂O nanoparticles onto the surface of MXene, to prevent the self-restacking of MXene nanosheets, and to create more active sites for electrochemical reactions. Furthermore,

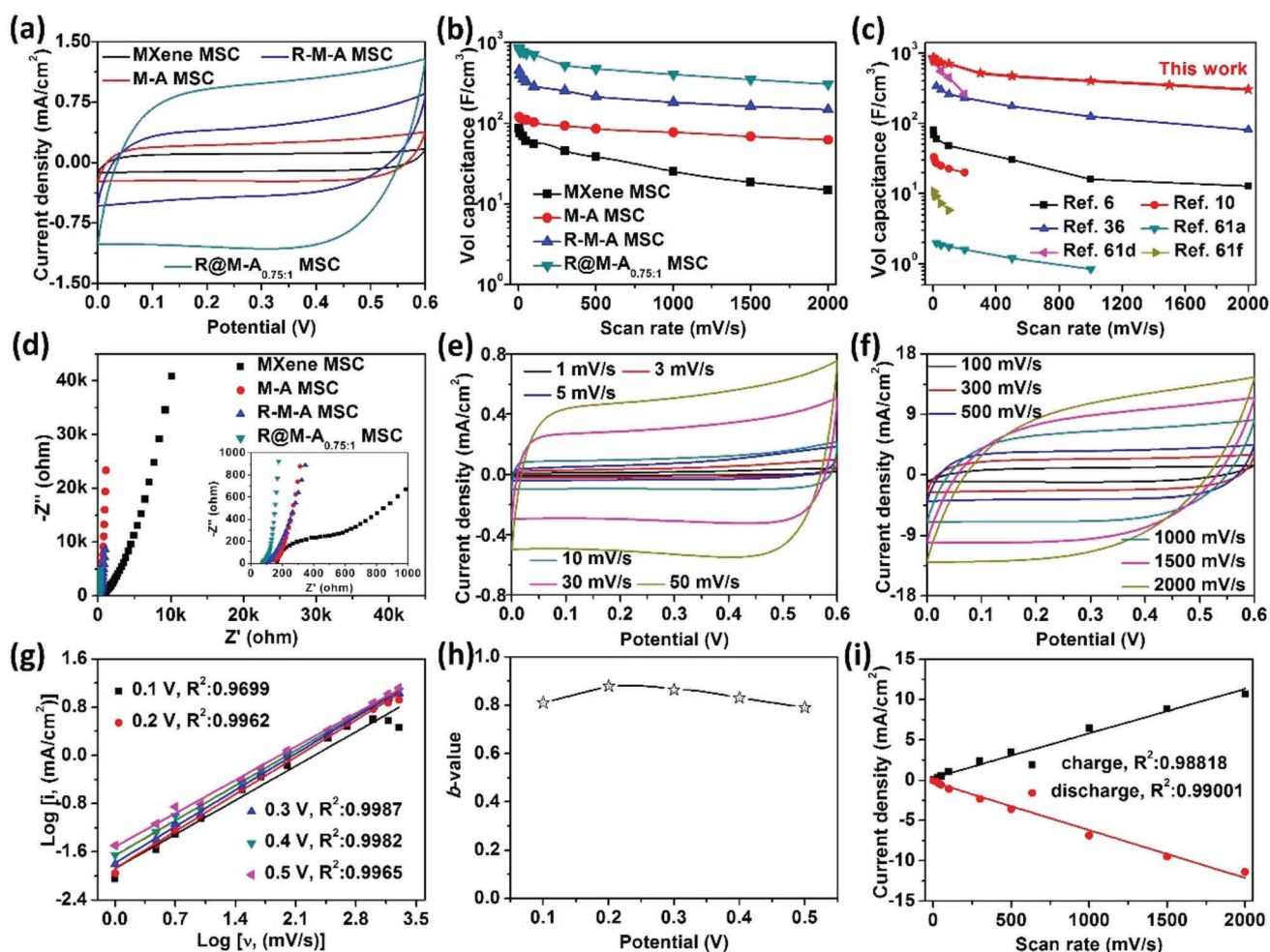


Figure 5. Comparison of the a) CV curves at a scan rate of 100 mV s^{-1} and b) volumetric capacitances at different scan rates of the MXene MSC, M-A MSC, R-M-A MSC, and R@M-A_{0.75:1} MSC. c) The volumetric specific capacitance of R@M-A_{0.75:1} MSC calculated from different scan rates in comparison to other state-of-the-art MXene-based MSCs. d) Nyquist plots of a MXene MSC, M-A MSC, R-M-A MSC, and R@M-A_{0.75:1} MSC. Electrochemical performances of R@M-A_{0.75:1} MSC: CV curves at different scan rates from e) 1 to 50 mV s^{-1} and f) 100 to 2000 mV s^{-1} , g) logarithm current response plotted against logarithm scan rate at different voltages for the determination of b -values, h) variation of b -values as a function of potential, and i) the linear relationship between the current density (extracted from CV curves at 0.3 V for both charge and discharge processes) and scan rates.

these uniformly dispersed hydrous RuO₂ nanoparticles complete the reaction with the electrolyte during the electrochemical redox process, which originates from the surface of the hydrous RuO₂ nanoparticles. This process greatly improves the utilization rate of the electrode. As a result, the R@M-A_{0.75:1} MSC is capable of achieving remarkably high volumetric capacitances coupled with a high rate capability.

To further understand the charge storage mechanism of the four types of MSCs, sweep analysis was performed at different scan rates to study the diffusion-controlled contribution and the capacitive contribution to the total charge storage. Figure 5e,f and Figure S8 (Supporting Information) show the CV curves of the four MSCs at different scan rates. The CV curves of R@M-A_{0.75:1} MSC exhibit a highly rectangular shape at a low scan rate, maintaining its shape even at a high scan rate of 2000 mV s^{-1} . The measured current (i) at 0.3 V from CV curves obeys the power law relationship with the scan rate (v), and can be expressed as follows^[64]

$$i = av^b \quad (3)$$

$$\log i = \log a + b \log v \quad (4)$$

where a is constant, v is the scan rate, and b is a value ranging from 0.5 (diffusion-controlled contribution) to 1 (capacitive contribution). A b -value of 0.5 indicates that the current is controlled by semi-infinite linear diffusion, while a b -value of 1 indicates that the current is surface-controlled.^[65] In general, the smaller the b -value is, the larger the contribution from diffusion-controlled intercalation processes, while the larger the b -value, the larger the capacitive contribution. As can be seen from Figure 5g and Figure S8 (Supporting Information), the b values of all MSCs are larger than 0.5 and close to 1, which contributes to the high capacitance of the screen-printed MSCs. However, the comparatively lower b -value of the pure MXene MSC indicates a relatively lower capacitive contribution and

poor rate capability, which is physically manifested by slower electron transfer and a longer ion diffusion length.^[25] The b -values of R@M-A_{0.75:1} MSC obtained at different potentials fall in the range of 0.79–1, as shown in Figure 5g,h. This b -value range signifies that the response is predominantly capacitive in the potential window. An in-depth exploration of the relationship between the current response and the scan rate of R@M-A_{0.75:1} MSC is presented in Figure 5i. It can be observed that the current density at 0.3 V increases approximately linearly at the scan rate range between 1 and 2000 mV s⁻¹. Furthermore, a strong linear relationship with R^2 between 0.98818 and 0.99001 is observed during charging and discharging, demonstrating its high power output capability due to the fast charge transport and the diffusion of the electrolyte.^[66]

Figure 6a,b illustrates the galvanostatic charge/discharge (GCD) curves of the R@M-A_{0.75:1} MSC at different current densities ranging from 0.1 to 4.0 mA cm⁻², respectively. The curves display a symmetrical triangular shape with an inappreciable

deviation, indicating excellent capacitive behavior and Coulombic efficiency of this device, which align well with the results from the CV tests. Based on the discharging behavior observed in the GCD curve, the volumetric capacitance of R@M-A_{0.75:1} MSC was determined to be 267.9 F cm⁻³ at a current density of 0.1 mA cm⁻² (Figure 6c). At higher current densities of 4.0 mA cm⁻², the MSC still maintained a volumetric capacitance of 161.7 F cm⁻³, representing an 83% retention of Coulombic efficiency. High volumetric energy and power densities of microscale energy storage devices are necessary for flexible and wearable electronics.^[67] To further quantify, Ragone plots related to volumetric energy and power densities of the R@M-A_{0.75:1} MSC were compared to the state-of-the-art MXene-based MSCs, as shown in Figure 6d. The R@M-A_{0.75:1} MSC exhibited energy density values in the range of 8.1–13.5 mWh cm⁻³ with corresponding power densities in the range of 1.1–48.5 W cm⁻³. These values are one order of magnitude higher than those of commercially available supercapacitors (2.75 V/44 mF and

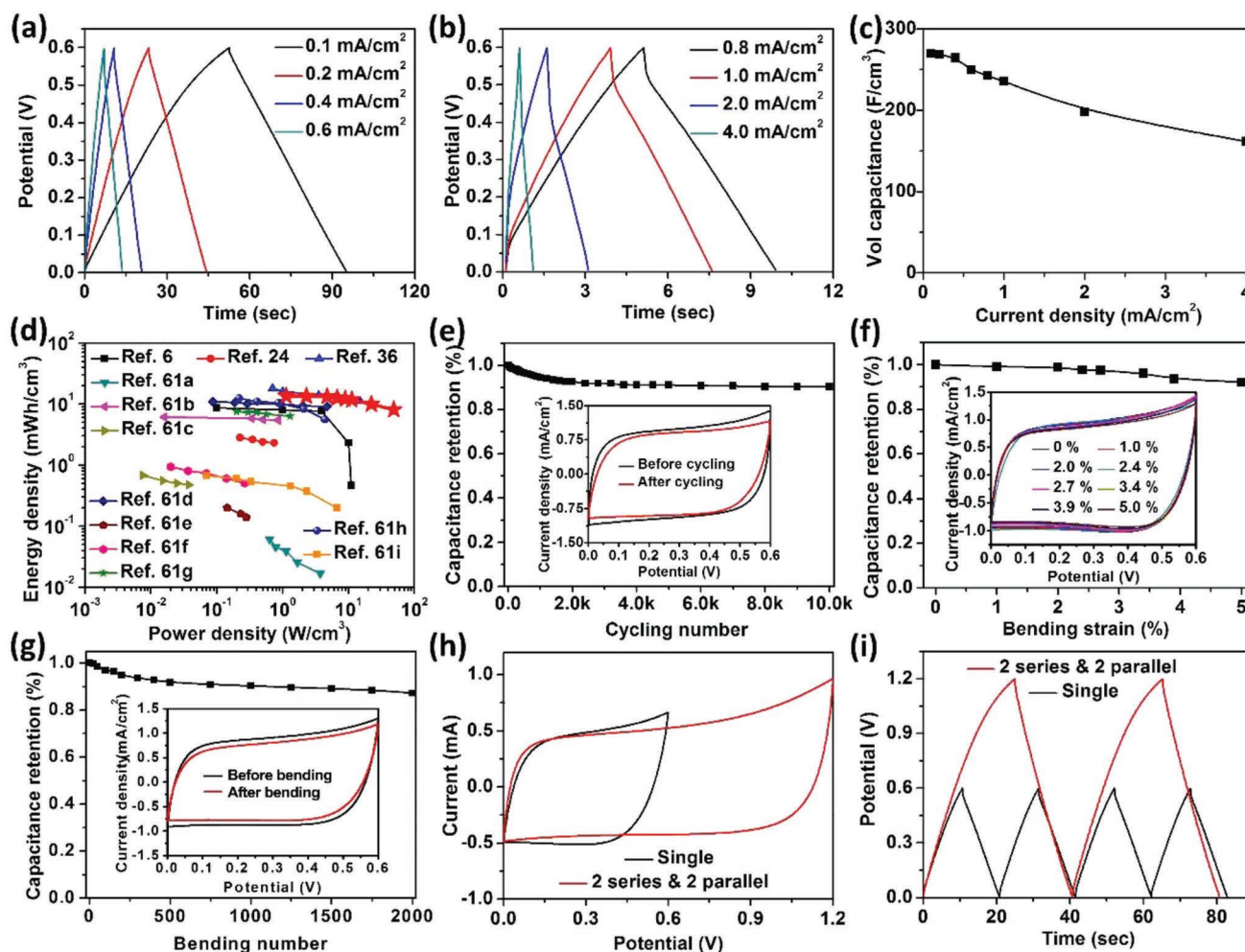


Figure 6. Electrochemical performance of R@M-A_{0.75:1} MSC: GCD profiles at different current densities ranging from a) 0.1 to 0.6 mA cm⁻² and b) 0.8 to 4.0 mA cm⁻², c) the volumetric specific capacitance obtained at different current densities, d) Ragone plot in comparison with other state-of-the-art MXene-based MSCs, e) cycling stability measured at a fixed scan rate of 100 mV s⁻¹ (inset: CV curves before and after cycling), f) capacitance retention under different bending strains (inset: CV curves obtained at different bending strains, at 100 mV s⁻¹), and g) capacitance retention at different bending cycles to a bending strain of 5.0% (inset: contrastive CV curves recorded at 100 mV s⁻¹ before and after 2000 bending cycles). h) CV curves tested at 100 mV s⁻¹ and i) GCD curves of the R@M-A_{0.75:1} MSCs connected in parallel and in series at a current density of 0.4 mA cm⁻², compared to curves taken of a single microdevice.

5.5 V/100 mF, $<1 \text{ mWh cm}^{-3}$),^[1] superior to those of Li-based thin-film batteries (10 mWh cm^{-3}),^[8] and are comparable or larger than those of MXene-based MSCs^[61] and the MSCs fabricated by printing techniques,^[62] as shown in Tables S1 and S2 (Supporting Information). Furthermore, as a demonstration of the real-world applicability of the device, the long-term cycling stability of the R@M-A_{0.75:1} MSC was tested at 100 mV s^{-1} for 10 000 cycles. It is observed from Figure 6e that $\approx 90\%$ of the initial capacitance is maintained after these 10 000 cycles. This long-term ability was further validated by postmortem analysis of the MSC electrodes, which show that the structure of the AgNW network is not destroyed after cycling (Figure S9, Supporting Information). Nevertheless, MXene can be oxidized in aqueous electrolytes with oxygen,^[6] which could result in the degeneration of the capacitance during the cyclic measurement.

In order to meet the urgent need for mechanical flexibility and shape diversity of future electronic products, innovative smart power source systems are highly required to be shape conformable yet mechanically flexible, and are also seamlessly integrated with these electronic devices.^[68] To evaluate the mechanical robustness of the screen-printed microdevices, CV measurements were conducted to probe the electrochemical performance of the R@M-A_{0.75:1} MSC under different bending strains ranging from 0% to 5.0%. As illustrated in Figure 6f, only slight capacitance changes were observed upon bending, with $\approx 92.1\%$ of the initial capacitance remaining even at a bending strain of 5.0%. Furthermore, the R@M-A_{0.75:1} MSC demonstrated mechanical robustness, maintaining nearly 87.3% of its original capacitance after 2000 bending cycles under a bending strain of 5.0% (Figure 6g). After repeated bending tests, no delamination appeared but only a few microcracks are formed on the microelectrode (Figure S10, Supporting Information), which may be the main cause for capacitance degradation. This mechanical compliancy and robustness is attributed to the network structure of the AgNWs soldered by the flexible yet tough RuO₂·xH₂O@MXene nanosheets assembled within the printed electrodes. This structure enables the system to accommodate the applied strain, resulting in mechanical flexibility and durability.

The R@M-A_{0.75:1} ink utilized as an electrode for MSC exhibits excellent electrical conductivity and electrochemical performance for MSCs. As such, this conductive and stable ink can simultaneously act as microelectrodes and interconnects for the scalable production of MSCs. As a demonstration of this feasibility, two R@M-A_{0.75:1} MSCs connected in series and in parallel were fabricated and characterized by CV and GCD profiles. The two series-connected MSCs increase the voltage window by a factor of two (Figure S11a, Supporting Information), while the capacitance is halved compared to that of a single device (Figure S11b, Supporting Information). The two parallel-connected MSCs double the capacitance when compared to that of a single device, while still retaining the same operating voltage window (Figure S11c,d, Supporting Information). When taken one step further, the MSC array constructed with two in parallel and two in series exhibited not only the stepwise increase in voltage from 0.6 to 1.2 V (Figure 6h), but also double the current output and discharge time (Figure 6i). These empirical demonstrations highlight the potential of these screen-printed MSCs to serve as next-generation, intelligent,

micro power source units for seamless integration into shape-conformable electronics requiring variable operation voltage and capacitance.

3. Conclusion

A facile screen-printing method for the fabrication of fully printed, in-plane, flexible MSCs on paper substrates was demonstrated using a thixotropic electrode ink comprising all-pseudocapacitive hydrous RuO₂-anchored Ti₃C₂T_x MXene nanocomposite and highly conductive 1D AgNWs. The MXene nanosheets are separated by hydrous RuO₂ nanoparticles anchored onto the surface of the nanosheets through oxygen-containing functional groups. Due to the amalgamation of properties and the synergistic effects stemming from the individual constituents, the flexible MSCs demonstrated high printing resolution, high electrochemical performance with regard to volumetric capacitance, and energy and power density, excellent cycling stability, and durable and robust mechanical properties. This simple, scalable, and repeatable one-step screen-printing strategy opens up a new avenue for the fabrication of high-performance, miniaturized, and printed portable and wearable on-chip electronic devices in a facile, versatile, and scalable process.

4. Experimental Section

Preparation of Delaminated Ti₃C₂T_x: 2.0 g of LiF (Sigma Aldrich) was added to 20 mL of 9 M HCl (Sigma Aldrich), followed by ultrasonic treatment for 30 min to homogeneously mix the two materials.^[6,19] Following the ultrasonic treatment, 1.0 g Ti₃AlC₂ powder was slowly added into the aforementioned solution and magnetically stirred for 24 h at 35 °C. The acidic suspension was washed with deionized (DI) water and centrifuged at 3500 rpm multiple times (5 min per cycle) until a pH ≥ 6 was obtained. The stable dark green supernatant of delaminated Ti₃C₂T_x was collected after strong agitation using a VORTEX mixer at 1000 rpm for 0.5 h and 30 min of centrifuging at 3500 rpm. The resultant Ti₃C₂T_x colloidal suspension was freeze-dried to obtain Ti₃C₂T_x powder.

Preparation of Amorphous Hydrous RuO₂ Nanoparticles: 40 mL of a 2 mg mL⁻¹ anhydrous ruthenium chloride (RuCl₃, Beijing HWRK Chem Co., Ltd.) solution was added to a 100 mL vial and heated to 95 °C for 18 h under magnetic stirring at 350 rpm.^[40] After cooling to room temperature, the product was collected after centrifugation and washed with DI water. The resultant precipitation was sonochemically treated for 30 min to ensure uniform dispersion, resulting in a 5 mg mL⁻¹ hydrous RuO₂ nanoparticles colloidal solution.

Preparation of RuO₂·xH₂O@MXene Nanocomposite: In a typical preparation, 100 mg of delaminated Ti₃C₂T_x MXene powder was first dispersed in 50 mL of deoxygenated DI water. After mild sonochemical treatment for 1 min, 39 mL of a 2 mg mL⁻¹ anhydrous RuCl₃ deoxygenated aqueous solution was slowly added into the Ti₃C₂T_x MXene dispersed solution under magnetic stirring. The reacted sample was transferred to a 250 mL round bottom (RB) flask and heated at 95 °C for 18 h under magnetic stirring at 350 rpm in N₂ atmosphere. Following heat treatment, the reacted product was centrifuged and washed with DI water several times. The resultant precipitation was agitated with a VORTEX mixer and sonochemically treated for 2 min to result in a 10 mg mL⁻¹ RuO₂·xH₂O@MXene nanocomposite colloidal solution.

Preparation of RuO₂·xH₂O@MXene-AgNW inks: RuO₂·xH₂O@MXene-AgNW inks were prepared according to our previously published works.^[33,34] In detail, the RuO₂·xH₂O@MXene and AgNW aqueous dispersions were mixed and uniformly dispersed through

intermittent strong agitation and ultrasonic treatment for 5 min. The wt% of RuO₂·xH₂O@MXene in the mixture was 33%, 43%, and 50%, corresponding to a weight ratio of RuO₂·xH₂O to AgNWs of 0.5:1, 0.75:1, and 1:1, respectively. Following mixture, the aqueous dispersion was first vacuum filtrated with a PTFE filter membrane with a pore size of 0.45 μm, then washed with 100 mL DI water five times. The collected RuO₂·xH₂O@MXene–AgNW filter cake on the filter membrane was re-dispersed in distilled water through strong agitation at 1000 rpm for 0.5 h to obtain the final homogeneous printable RuO₂·xH₂O@MXene–AgNW gel-like ink. The resulting inks are denoted as RuO₂·xH₂O@MXene–AgNW_{0.5:1}, RuO₂·xH₂O@MXene–AgNW_{0.75:1}, and RuO₂·xH₂O@MXene–AgNW_{1:1} ink, corresponding to their ratio of RuO₂·xH₂O to AgNWs. For comparison, a pure MXene ink, MXene–AgNW (0.75:1, wt%) ink and RuO₂·xH₂O nanoparticles–MXene–AgNW (0.25:0.5:1, wt%) ink were also made according to the aforementioned process.

Preparation of the Gel Electrolyte: The PVA–KOH gel electrolyte was prepared by first adding 3 g of PVA (*M_w* = 120 000, Sigma-Aldrich) into 20 mL DI water. The mixture was subsequently transferred to an RB flask and heated to 90 °C under constant stirring until the solution became transparent. After heating, 3.0 g KOH diluted in 10 mL of DI water was added to the PVA solution and stirred for 2 h. The final solution was cooled to room temperature and dropped onto the interdigital pattern area of the printed MSCs to fully wet the electrode. The coated solution was dried under ambient conditions to solidify the electrolyte.

Preparation of Screen-Printed Flexible MSCs: The screen-printing process was conducted on a TC-4060k screen printer purchased from Dongguan Ta Chen Screen Printing Machine & Materials Co., Ltd. The screen-printing device comprises a rubber squeegee, a 500 mesh count precision stainless-steel screen mesh from Dongguan Xiang Peng Screen Printing Equipment Co., Ltd., and a base plate. To print, the screen mesh (18 μm wire diameter, 33 μm mesh opening, 45° mesh angle, standard mesh tension, 8 μm emulsion thickness) with the appropriate pattern was first installed in the printer. Following installation, the pattern was generated by spreading the prepared gel-like ink onto the screen mesh. The printing speed, printing force, and angle between the rubber squeegee and screen mesh were specifically optimized for different screen-printed inks. MSCs were printed by sliding the squeegee over the stencil, followed by drying under ambient condition for 3–5 min. The area value of the printed MSCs is calculated to be 0.47615 cm² (Supporting Information). About 25 μL PVA–KOH gel electrolyte was then dropped to cover the whole MSC to complete the device construction. Lastly, PDMS (silicone elastomer base:silicone elastomer curing agent = 10:1 in weight) was used as a passivation layer to cover the gel electrolyte for enhanced stability.

Characterization: SEM characterizations were carried out using a field-emission scanning electron microscopy (JSM-7800) at an accelerating voltage of 5.0 kV. TEM images were captured using a JEM-2010 system from JEOL. AFM images were taken with a MultiMode 8 system from Bruker. XRD patterns of the samples were obtained from a Rigaku D/max 2200 pc diffractometer using Cu Kα radiation. The nitrogen adsorption–desorption analysis was conducted by using an automatic N₂ adsorption–desorption instrument (ASAP TriStar II 3020, Micromeritics Inc., USA) at 77 K. The specific surface areas of the different nanopowders were calculated using the BET method. Pore size distributions were obtained from the desorption branch using the Barrette–Joynere–Halenda (BJH) model. XPS characterization was conducted using an ESCALAB 250Xi system from Thermo Scientific. The electrical conductivity was measured by digital and intelligent four-probe meter (ST2258C). Optical microscopy images and digital camera images of the samples were taken with a Leica DM750 M and Canon 5D Mark III, respectively.

The rheological properties of the screen-printing inks were probed using a DHR-2 rheometer (TA Instruments) with a 20 mm parallel plate geometry and 800 μm gap. All measurements were taken at 25 °C. Before each test, a preconditioning step at a shear rate of 0.1 s^{−1} for 10 s was applied. The apparent viscosity of inks was

investigated at shear rates ranging from 0.1 to 1000 s^{−1}. The PHS test was performed at constant shear rates in the following stepwise function: 0.1 s^{−1} shear rate for 30 s, 200 s^{−1} for 30 s, and 0.1 s^{−1} for 120 s, to simulate the screen-printing process. A stress sweep step (SSS) test was performed with oscillation stress ranging from 1 to 1000 Pa at a frequency of 1 Hz.

All electrochemical measurements were carried out in a two-electrode system using an electrochemical workstation (CHI 660D, CH Instruments, Inc.), with all tests conducted at room temperature. EIS was carried out at the open circuit potential with a 5 mV amplitude in a frequency range of 0.01 Hz to 100 kHz.

Calculations: The capacitance values were calculated from the CV curves by integrating the discharge portion according to the following equation^[69,70]

$$C = \frac{1}{v(V_f - V_i)} \int_{V_i}^{V_f} I(V) dV \quad (5)$$

where *V_f* and *V_i* are the integration potential limits of the voltammetric curve, *v* is the scan rate (V s^{−1}), and *I(V)* is the voltammetric discharge current (A).

The capacitance values were calculated from the GCD curves from the following equation

$$C = (I \times \Delta t) / \Delta V \quad (6)$$

where *I* is the discharge current (A), *Δt* is the discharge time (s), and *ΔV* is the discharge potential range (V).

Volumetric specific capacitances *C_{vol}* (F cm^{−3}) of the MSC device were calculated based on the volume of the device according to Equations (7)

$$C_{vol} = C / V_{device} \quad (7)$$

The *V_{device}* refer to the total volume of the device (including the interdigitated electrodes and the interspacing between them).

Volumetric energy density (*E*) and power density (*P*) of the MSC device are calculated according to Equations (8) and (9), respectively

$$E = \frac{1}{2} \times C_{vol} \times \frac{(\Delta V)^2}{3600} \quad (8)$$

$$P = \frac{E}{\Delta t} \times 3600 \quad (9)$$

where *E* is the volumetric energy density (Wh cm^{−3}), *P* is the volumetric power density (W cm^{−3}), *C_{vol}* is the volumetric specific capacitance obtained from formula (7), *ΔV* is the discharge potential range (V), and *Δt* is the discharge time (s).

Supporting Information

Supporting Information is available from the Wiley Online Library or from the author.

Acknowledgements

The work reported here was supported by NSFC (51872146, 51673099, 91633301, 21421001), Tianjin Municipal Science and Technology Commission (17JZDJC30200) in China, and MoST (2016YFA0200200).

Conflict of Interest

The authors declare no conflict of interest.

Keywords

flexible micro-supercapacitors, MXene, ruthenium(IV) oxide nanoparticles, screen printing, silver nanowires

Received: December 26, 2018

Revised: January 31, 2019

Published online: February 25, 2019

- [1] D. Yu, K. Goh, H. Wang, L. Wei, W. Jiang, Q. Zhang, L. Dai, Y. Chen, *Nat. Nanotechnol.* **2014**, *9*, 555.
- [2] M. Beidaghi, Y. Gogotsi, *Energy Environ. Sci.* **2014**, *7*, 867.
- [3] Y. Da, J. Liu, L. Zhou, X. Zhu, X. Chen, L. Fu, *Adv. Mater.* **2019**, *31*, 1802793.
- [4] X. Shi, S. Pei, F. Zhou, W. Ren, H. Cheng, Z. Wu, X. Bao, *Energy Environ. Sci.* **2019**, <https://doi.org/10.1039/C8EE02924E>.
- [5] D. Qi, Y. Liu, Z. Liu, L. Zhang, X. Chen, *Adv. Mater.* **2017**, *29*, 1602802.
- [6] Y.-Y. Peng, B. Akuzum, N. Kurra, M.-Q. Zhao, M. Alhabeab, B. Anasori, E. C. Kumbur, H. N. Alshareef, M.-D. Ger, Y. Gogotsi, *Energy Environ. Sci.* **2016**, *9*, 2847.
- [7] K. Wang, W. Zou, B. Quan, A. Yu, H. Wu, P. Jiang, Z. Wei, *Adv. Energy Mater.* **2011**, *1*, 1068.
- [8] M. F. El-Kady, R. B. Kaner, *Nat. Commun.* **2013**, *4*, 1475.
- [9] N. A. Kyeremateng, T. Brousse, D. Pech, *Nat. Nanotechnol.* **2016**, *12*, 7.
- [10] H. Hu, Z. Bai, B. Niu, M. Wu, T. Hua, *J. Mater. Chem. A* **2018**, *6*, 14876.
- [11] Z. H. Nie, E. Kumacheva, *Nat. Mater.* **2008**, *7*, 277.
- [12] M. Naguib, M. Kurtoglu, V. Presser, J. Lu, J. Niu, M. Heon, L. Hultman, Y. Gogotsi, M. W. Barsoum, *Adv. Mater.* **2011**, *23*, 4248.
- [13] M. Naguib, O. Mashtalir, J. Carle, V. Presser, J. Lu, L. Hultman, Y. Gogotsi, M. W. Barsoum, *ACS Nano* **2012**, *6*, 1322.
- [14] C. Xu, L. Wang, Z. Liu, L. Chen, J. Guo, N. Kang, X.-L. Ma, H.-M. Cheng, W. Ren, *Nat. Mater.* **2015**, *14*, 1135.
- [15] M. R. Lukatskaya, O. Mashtalir, C. E. Ren, Y. Dall'Agnese, P. Rozier, P. L. Taberna, M. Naguib, P. Simon, M. W. Barsoum, Y. Gogotsi, *Science* **2013**, *341*, 1502.
- [16] H. Wang, Y. Wu, X. Yuan, G. Zeng, J. Zhou, X. Wang, J. W. Chew, *Adv. Mater.* **2018**, *30*, 1704561.
- [17] M. R. Lukatskaya, S. Kota, Z. Lin, M.-Q. Zhao, N. Shpigel, M. D. Levi, J. Halim, P.-L. Taberna, M. W. Barsoum, P. Simon, Y. Gogotsi, *Nat. Energy* **2017**, *2*, 17105.
- [18] B. Anasori, M. R. Lukatskaya, Y. Gogotsi, *Nat. Rev. Mater.* **2017**, *2*, 16098.
- [19] Z. Fan, Y. Wang, Z. Xie, D. Wang, Y. Yuan, H. Kang, B. Su, Z. Cheng, Y. Liu, *Adv. Sci.* **2018**, *5*, 1800750.
- [20] W. Liu, Z. Wang, Y. Su, Q. Li, Z. Zhao, F. Geng, *Adv. Energy Mater.* **2017**, *7*, 1602834.
- [21] Y. Tian, C. Yang, W. Que, X. Liu, X. Yin, L. B. Kong, *J. Power Sources* **2017**, *359*, 332.
- [22] M. Q. Zhao, C. E. Ren, Z. Ling, M. R. Lukatskaya, C. Zhang, K. L. Van Aken, M. W. Barsoum, Y. Gogotsi, *Adv. Mater.* **2015**, *27*, 339.
- [23] X. Xie, M. Q. Zhao, B. Anasori, K. Maleski, C. E. Ren, J. Li, B. W. Byles, E. Pomerantseva, G. Wang, Y. Gogotsi, *Nano Energy* **2016**, *26*, 513.
- [24] H. Li, Y. Hou, F. Wang, M. R. Lohe, X. Zhuang, L. Niu, X. Feng, *Adv. Energy Mater.* **2017**, *7*, 1601847.
- [25] J. Yan, C. E. Ren, K. Maleski, C. B. Hatter, B. Anasori, P. Urbankowski, A. Sarycheva, Y. Gogotsi, *Adv. Funct. Mater.* **2017**, *27*, 1701264.
- [26] M. Boota, B. Anasori, C. Voigt, M. Q. Zhao, M. W. Barsoum, Y. Gogotsi, *Adv. Mater.* **2016**, *28*, 1517.
- [27] M. Zhu, Y. Huang, Q. Deng, J. Zhou, Z. Pei, Q. Xue, Y. Huang, Z. Wang, H. Li, Q. Huang, C. Zhi, *Adv. Energy Mater.* **2016**, *6*, 1600969.
- [28] C.-F. Du, Q. Liang, Y. Zheng, Y. Luo, H. Mao, Q. Yan, *ACS Appl. Mater. Interfaces* **2018**, *10*, 33779.
- [29] J. Y. Hwang, M. F. El-Kady, Y. Wang, L. Wang, Y. Shao, K. Marsh, J. M. Ko, R. B. Kaner, *Nano Energy* **2015**, *18*, 57.
- [30] Z.-S. Wu, D.-W. Wang, W. Ren, J. Zhao, G. Zhou, F. Li, H.-M. Cheng, *Adv. Funct. Mater.* **2010**, *20*, 3595.
- [31] H. Wang, J. T. Robinson, G. Diankov, H. Dai, *J. Am. Chem. Soc.* **2010**, *132*, 3270.
- [32] H. Tang, W. Li, L. Pan, C. P. Cullen, Y. Liu, A. Pakdel, D. Long, J. Yang, N. McEvoy, G. S. Duesberg, V. Nicolosi, C. Zhang, *Adv. Sci.* **2018**, *5*, 1800502.
- [33] X. L. Shi, S. R. Liu, Y. Sun, J. J. Liang, Y. S. Chen, *Adv. Funct. Mater.* **2018**, *28*, 1800850.
- [34] S. Liu, X. Shi, X. Li, Y. Sun, J. Zhu, Q. Pei, J. Liang, Y. Chen, *Nanoscale* **2018**, *10*, 20096.
- [35] A. Lipatov, M. Alhabeab, M. R. Lukatskaya, A. Boson, Y. Gogotsi, *Adv. Electron. Mater.* **2016**, *2*, 1600255.
- [36] C. J. Zhang, M. P. Kremer, A. Seral-Ascaso, S.-H. Park, N. McEvoy, B. Anasori, Y. Gogotsi, V. Nicolosi, *Adv. Funct. Mater.* **2018**, *28*, 1705506.
- [37] X. Zhang, R. Lv, A. Wang, W. Guo, X. Liu, J. Luo, *Angew. Chem., Int. Ed.* **2018**, *57*, 15028.
- [38] J. Cao, C. Chen, Q. Zhao, N. Zhang, Q. Lu, X. Wang, Z. Niu, J. Chen, *Adv. Mater.* **2016**, *28*, 9629.
- [39] C. Yang, Y. Tang, Y. Tian, Y. Luo, M. F. U. Din, X. Yin, W. Que, *Adv. Energy Mater.* **2018**, *8*, 1802087.
- [40] J. Lee, S. A. S. Shah, P. J. Yoo, B. Lim, *Chem. Phys. Lett.* **2017**, *673*, 89.
- [41] K.-H. Chang, C.-C. Hu, C.-Y. Chou, *Chem. Mater.* **2007**, *19*, 2112.
- [42] Y. Wang, H. Dou, J. Wang, B. Ding, Y. Xu, Z. Chang, X. Hao, *J. Power Sources* **2016**, *327*, 221.
- [43] J. Liu, H. Li, H. Zhang, Q. Liu, R. Li, B. Lia, J. Wang, *J. Solid State Chem.* **2018**, *257*, 64.
- [44] S. Niu, Z. Wang, M. Yu, M. Yu, L. Xiu, S. Wang, X. Wu, J. Qiu, *ACS Nano* **2018**, *12*, 3928.
- [45] Q. Xue, Z. Pei, Y. Huang, M. Zhu, Z. Tang, H. Li, Y. Huang, N. Li, H. Zhang, C. Zhi, *J. Mater. Chem. A* **2017**, *5*, 20818.
- [46] C. Zeng, F. Xie, X. Yang, M. Jaroniec, L. Zhang, S.-Z. Qiao, *Angew. Chem., Int. Ed.* **2018**, *57*, 8540.
- [47] Z. J. Han, S. Pineda, A. T. Murdock, D. H. Seo, K. (Ken) Ostrikovb, A. Bendavid, *J. Mater. Chem. A* **2017**, *5*, 17293.
- [48] W. Wang, S. Guo, I. Lee, K. Ahmed, J. Zhong, Z. Favors, F. Zaera, M. Ozkan, C. S. Ozkan, *Sci. Rep.* **2015**, *4*, 4452.
- [49] Y.-T. Liu, P. Zhang, N. Sun, B. Anasori, Q.-Z. Zhu, H. Liu, Y. Gogotsi, B. Xu, *Adv. Mater.* **2018**, *30*, 1707334.
- [50] S. D. Lacey, D. J. Kirsch, Y. Li, J. T. Morgenstern, B. C. Zarket, Y. Yao, J. Dai, L. Q. Garcia, B. Liu, T. Gao, S. Xu, S. R. Raghavan, J. W. Connell, Y. Lin, L. Hu, *Adv. Mater.* **2018**, *30*, 1705651.
- [51] Z. Xiong, C. Liao, W. Han, X. Wang, *Adv. Mater.* **2015**, *27*, 4469.
- [52] J. Liang, K. Tong, Q. Pei, *Adv. Mater.* **2016**, *28*, 5986.
- [53] H. Xiao, Z. S. Wu, L. Chen, F. Zhou, S. Zheng, W. Ren, H. M. Cheng, X. Bao, *ACS Nano* **2017**, *11*, 7284.
- [54] K.-H. Choi, J. T. Yoo, C. K. Lee, S.-Y. Lee, *Energy Environ. Sci.* **2016**, *9*, 2812.
- [55] W. J. Hyun, E. B. Secor, C. H. Kim, M. C. Hersam, L. F. Francis, C. D. Frisbie, *Adv. Energy Mater.* **2017**, *7*, 1700285.
- [56] G. Liu, W. Jin, N. Xu, *Chem. Soc. Rev.* **2015**, *44*, 5016.
- [57] H. F. Li, R. D. Wang, R. Cao, *Microporous Mesoporous Mater.* **2008**, *111*, 32.
- [58] S.-Y. Lin, X. Zhang, *J. Power Sources* **2015**, *294*, 354.
- [59] C. Yang, Y. Tang, Y. Tian, Y. Luo, Y. He, X. Yin, W. Que, *Adv. Funct. Mater.* **2018**, *28*, 1705487.

- [60] Z. Peng, X. Liu, H. Meng, Z. Li, B. Li, Z. Liu, S. Liu, *ACS Appl. Mater. Interfaces* **2017**, *9*, 4577.
- [61] a) C. Couly, M. Alhabeb, K. L. Van Aken, N. Kurra, L. Gomes, A. M. Navarro-Suárez, B. Anasori, H. N. Alshareef, Y. Gogotsi, *Adv. Electron. Mater.* **2018**, *4*, 1700339; b) Q. Jiang, C. Wu, Z. Wang, A. C. Wang, J.-H. He, Z. L. Wang, H. N. Alshareef, *Nano Energy* **2018**, *45*, 266; c) N. Kurra, B. Ahmed, Y. Gogotsi, H. N. Alshareef, *Adv. Energy Mater.* **2016**, *6*, 1601372; d) H. Hu, Y. Hua, *J. Mater. Chem. A* **2017**, *5*, 19639; e) Q. Jiang, N. Kurra, M. Alhabeb, Y. Gogotsi, H. N. Alshareef, *Adv. Energy Mater.* **2018**, *8*, 1703043; f) B.-S. Shen, H. Wang, L.-J. Wu, R.-S. Guo, Q. Huang, X.-B. Yan, *Chin. Chem. Lett.* **2016**, *27*, 1586; g) S. Xu, W. Liu, X. Liu, X. Kuang, X. Wang, presented at 19th Int. Conf. on Solid-State Sensors, Actuators and Microsystems (TRANSDUCERS), Kaohsiung, Taiwan, June **2017**; h) H. Huang, H. Su, H. Zhang, L. Xu, X. Chu, C. Hu, H. Liu, N. Chen, F. Liu, W. Deng, B. Gu, H. Zhang, W. Yang, *Adv. Electron. Mater.* **2018**, *4*, 1800179; i) P. Salles, E. Quain, N. Kurra, A. Sarycheva, Y. Gogotsi, *Small* **2018**, *14*, 1802864.
- [62] a) Y. Wang, Y. Shi, C. X. Zhao, J. I. Wong, X. W. Sun, H. Y. Yang, *Nanotechnology* **2014**, *25*, 094010; b) Y. G. Zhu, Y. Wang, Y. Shi, J. I. Wong, H. Y. Yang, *Nano Energy* **2014**, *3*, 46; c) S. Liu, J. Xie, H. Li, Y. Wang, H. Y. Yang, T. Zhu, S. Zhang, G. Cao, X. Zhao, *J. Mater. Chem. A* **2014**, *2*, 18125; d) Y. Liu, B. Zhang, Q. Xu, Y. Hou, S. Seyedin, S. Qin, G. G. Wallace, S. Beirne, J. M. Razal, J. Chen, *Adv. Funct. Mater.* **2018**, *28*, 1706592; e) K. Shen, J. Ding, S. Yang, *Adv. Energy Mater.* **2018**, *8*, 1800408; f) W. Li, Y. Li, M. Su, B. An, J. Liu, D. Su, L. Li, F. Li, Y. Song, *J. Mater. Chem. A* **2017**, *5*, 16281; g) G. Sun, J. An, C. K. Chua, H. Pang, J. Zhang, P. Chen, *Electrochem. Commun.* **2015**, *57*, 33; h) L. Li, E. B. Secor, K. S. Chen, J. Zhu, X. Liu, T. Z. Gao, J.-W. T. Seo, Y. Zhao, M. C. Hersam, *Adv. Energy Mater.* **2016**, *6*, 1600909; i) J. Li, S. Sollami Delekta, P. Zhang, S. Yang, M. R. Lohe, X. Zhuang, X. Feng, M. Östling, *ACS Nano* **2017**, *11*, 8249; j) W. Liu, C. Lu, H. Li, R. Y. Tay, L. Sun, X. Wang, W. L. Chow, X. Wang, B. K. Tay, Z. Chen, J. Yan, K. Feng, G. Lui, R. Tjandra, L. Rasenthiram, G. Chiu, A. Yu, *J. Mater. Chem. A* **2016**, *4*, 3754; k) H. Pang, Y. Zhang, W.-Y. Lai, Z. Hu, W. Huang, *Nano Energy* **2015**, *15*, 303; l) H. Jung, C. Ve Cheah, N. Jeong, J. Lee, *Appl. Phys. Lett.* **2014**, *105*, 053902; m) Y. Xiao, L. Huang, Q. Zhang, S. Xu, Q. Chen, W. Shi, *Appl. Phys. Lett.* **2015**, *107*, 013906; n) Q. Zhang, L. Huang, Q. Chang, W. Shi, L. Shen, Q. Chen, *Nanotechnology* **2016**, *27*, 105401.
- [63] M. Cao, M. Wang, L. Li, H. Qiu, M. A. Padhiar, Z. Yang, *Nano Energy* **2018**, *50*, 528.
- [64] J. Wang, J. Polleux, J. Lim, B. Dunn, *J. Phys. Chem. C* **2007**, *111*, 14925.
- [65] J. Liu, W. Jin, C. Xu, J. Hao, C. Li, L. Zhang, J. Lin, Z. X. Shen, *Adv. Sci.* **2018**, *5*, 1700322.
- [66] Y. P. Fu, X. Cai, H. W. Wu, Z. B. Lv, S. C. Hou, M. Peng, X. Yu, D. C. Zou, *Adv. Mater.* **2012**, *24*, 5713.
- [67] X. W. Yang, C. Cheng, Y. F. Wang, L. Qiu, D. Li, *Science* **2013**, *341*, 534.
- [68] L. Wen, F. Li, H.-M. Cheng, *Adv. Mater.* **2016**, *28*, 4306.
- [69] X. Shi, Z.-S. Wu, J. Qin, S. Zheng, S. Wang, F. Zhou, C. Sun, X. Bao, *Adv. Mater.* **2017**, *29*, 1703034.
- [70] P. Zhang, Y. Li, G. Wang, F. Wang, S. Yang, F. Zhu, X. Zhuang, O. G. Schmidt, X. Feng, *Adv. Mater.* **2019**, *31*, 1806005.